




Experimental Determination of Phase Equilibria in the Mn-Zn Binary System

Daisuke Imatomi¹ · Ryosuke Ishikawa¹ · Akira Nakata¹ · Tatsuya Ito^{1,2} · Kwangsik Han^{1,3} · Makoto Nagasako⁴ · Xiao Xu^{1,5}  · Toshihiro Omori¹ · Ryosuke Kainuma¹

Submitted: 25 April 2023 / in revised form: 29 August 2023 / Accepted: 9 November 2023 / Published online: 15 December 2023
© The Author(s) 2023

Abstract Phase equilibria in the Mn-Zn binary system were experimentally determined by chemical composition examination, crystal structure determination, and thermal analysis. Major changes were detected for the β , ε , and δ phases. The β -B2 single-phase region could not be confirmed in the studied system because a disordered body-centered cubic structure, which is identical to the δ Mn phase, was confirmed in a quenched sample from the previously proposed region of β phase. The ε phase has been controversial whether the phase is separated into ε , ε_1 , and ε_2 phases or not. By studying a diffusion couple and several alloy compositions, it was established that the ε , ε_1 , and ε_2 phases are not separate and comprise a single ε phase. Furthermore, the δ phase is not present in the Zn-rich region of the system because the corresponding invariant reactions were not detected via thermal analysis.

Keywords coating materials · experimental phase equilibria · intermetallic compound · phase diagram

1 Introduction

High-manganese steels with twinning-induced plasticity (TWIP) behavior are widely used in automobile bodies because of their high strength and elongation.^[1–3] However, their inferior corrosion and oxidation resistance are problems to solve for practical applications. Therefore, hot-dip Zn coating processes such as hot-dip galvanizing (GI) and galvannealing (GA) are generally performed for these steels. During the GI process, a steel sheet is dipped into a Zn bath with a temperature of approximately 450 °C. In the case of the GA process, the Zn-plated steel sheet is further annealed at 500 °C to form the intermetallic compound (IMC) layers at the interface between the steel sheet and the molten Zn bath. During these processes, steels containing a large amount of Mn are known to show different types of IMCs compared to those in Fe-Zn; for example, the Γ phase that appears in the Fe-Zn system may be suppressed.^[4] The above-mentioned GI and GA processes, accompanied by the formation of various types of IMCs, involve non-equilibrium reactions and are not fully understood. Therefore, a precise determination of the phase diagrams of relevant elements is important; the phase diagrams reflect equilibrium conditions, but they provide basic information and are the starting points for the understanding of non-equilibrium reactions. Unfortunately, the Mn-Zn phase diagram, which is a fundamental binary system among the major components Fe, Zn, and Mn, remains controversial because contradictory experimental data were reported previously. In this study, the whole range of the phase diagram in the Mn-Zn system was determined.

✉ Xiao Xu
xu@material.tohoku.ac.jp

¹ Department of Materials Science, Graduate School of Engineering, Tohoku University, 6-6 Aramaki Aza Aoba, Aoba-ku, Sendai, Miyagi, Japan

² J-PARC Center, Japan Atomic Energy Agency, 2-4 Shirane Shirakata, Tokai-mura, Naka-gun, Ibaraki, Japan

³ Research Center for Structural Materials, National Institute for Materials Science, 1-2-1 Sengen, Tsukuba, Ibaraki, Japan

⁴ Institute for Materials Research, Tohoku University, 2-1-1 Katahira, Aoba-ku, Sendai, Miyagi, Japan

⁵ Organization for Advanced Studies, Tohoku University, 2-1-1 Katahira, Aoba-ku, Sendai, Miyagi, Japan

2 Literature Works

A phase diagram of the Mn–Zn binary system assessed by Okamoto and Tanner^[5] is shown in Fig. 1(a), and the crystal structures of its constituent phases are listed in Table 1.^[6–12] This assessed phase diagram is primarily based on the experimental data obtained by Wachtel and Tsiuplakis^[13] in the compositional range of 60 to 100Zn, by Romer and Wachtel^[14] from 0 to 60 Zn, and by Nakagawa and Hori^[15] from 30 to 70Zn below 400 °C (all the compositions in this work are reported in atomic percentages). For comparison, a partial phase diagram determined by Potter and Huber^[16] is also shown in Fig. 1(b).

By performing thermal analysis and x-ray diffraction (XRD), Potter and Huber^[16] reported that the δ Mn and β phases were separated by the γ Mn phase (Fig. 1b). Romer and Wachtel^[14] reported that these two phases neighbored each other through an order-disorder transformation according to thermal analysis data (Fig. 1a). Potter and Huber^[16] also established equilibria between the α Mn, β Mn, γ Mn, and δ Mn phases via x-ray analysis and microscopic observations (Fig. 1b). However, these results did not agree with the data obtained by Romer and Wachtel^[14] and Nakagawa and Hori^[15] (see Fig. 1a).

The liquidus and solidus lines related to δ Mn (and β) phases were determined by Siebe,^[17] Romer and Wachtel,^[14] and Schramm^[18] via thermal analysis, as shown in Fig. 1(a). These datasets are in good agreement with each other. However, different values of the invariant temperature for the reaction δ Mn + L \rightarrow ϵ were obtained by researchers. Romer and Wachtel^[14] and Wachtel and Tsiuplakis^[13] reported the value of 815 °C, whereas Schramm^[18] and Potter and Huber^[16] obtained the value of 835 °C.

The separation of the ϵ phase into the ϵ , ϵ_1 , and ϵ_2 phases remains a controversial topic. Wachtel and Tsiuplakis^[13] indicate phase separation as a change in the slope of isothermal magnetic susceptibility. Xu et al.^[19] also detected a concentration jump around the interface between ϵ and ϵ_1 phases using a diffusion couple (DC); however, they were unable to determine the two-phase boundaries even using electron probe microanalysis (EPMA). A phase diagram containing the separated ϵ , ϵ_1 , and ϵ_2 phases is presented in Fig. 1(a). In contrast, Henderson and Wilcox^[20] and Farrar and King^[21] measured the compositional dependence of the lattice parameters without detecting any anomalies related to phase separations. Furthermore, Romer and Wachtel^[14] examined a wide range of compositions related to ϵ , ϵ_1 , and ϵ_2 phases via isothermal magnetic susceptibility measurements. They found that the change of magnetic susceptibility was continuous with composition and did not observe any phase separations.

Phase equilibria between the liquidus and ϵ phase(s) have been examined by several researchers.^[13,14,17,22–25] These data have been used to determine the solidus and liquidus. Although the peritectic reactions of the L + ϵ_1 \rightarrow ϵ_2 and L + ϵ \rightarrow ϵ_1 were observed by Wachtel and Tsiuplakis,^[13] Parravano and Perret,^[22] Gieren,^[25] and Ackerman,^[23] these reactions were not reported by other researchers.

In addition, some groups established equilibria between the solid phases in the Zn-rich region. Their findings are briefly summarized below.

Schramm^[18] confirmed the phase boundaries around the α' phase via thermal analysis and XRD. Subsequently, Nakagawa and Hori^[15] determined the composition range in the Mn-rich region of the α' phase at 150 °C. Uchishiba et al.^[26] investigated the phase transition between the cubic α' and tetragonal α'_1 phase via thermal analysis (Note the

Fig. 1. (a) Phase diagram of the Mn–Zn binary system constructed by Okamoto and Tanner based on experimental data.^[5] (b) Partial phase diagram of the Mn-rich region determined by Potter and Huber^[16]

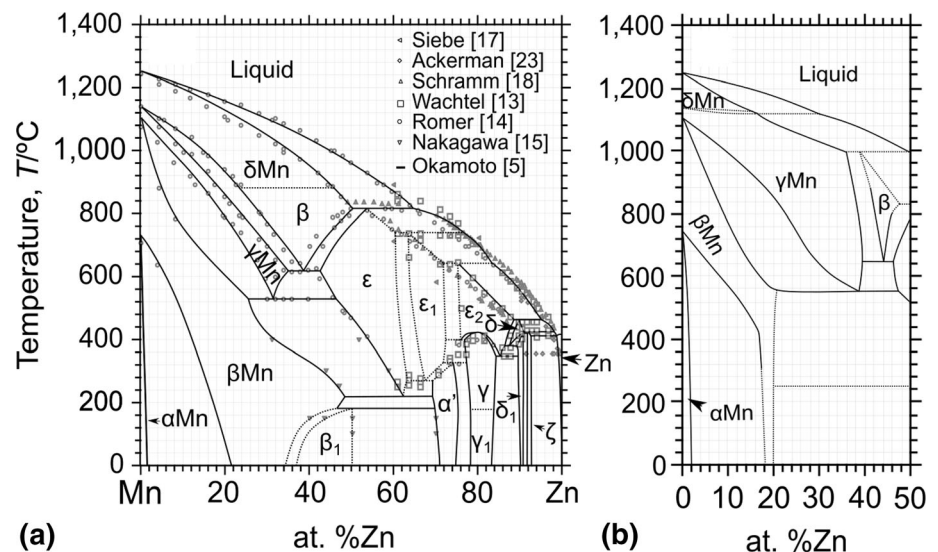


Table 1 Crystallographic information of the known solid solution phases and intermetallic compounds in the Mn-Zn binary system

Phase	Pearson symbol	Space group	Strukturbericht designation	Prototype	References
δ Mn	<i>cI2</i>	<i>Im$\bar{3}m$</i>	A2	W	Ref. 6
γ Mn	<i>cF4</i>	<i>Fm$\bar{3}m$</i>	A1	Cu	Ref. 6
β Mn	<i>cP20</i>	<i>P4₁32</i>	A13	β Mn	Ref. 6
α Mn	<i>cI58</i>	<i>I$\bar{4}3m$</i>	A12	α Mn	Ref. 6
β	<i>cP2</i>	<i>Pm$\bar{3}m$</i>	B2	CsCl	Ref. 7
β_1	<i>cP2</i>	<i>Pm$\bar{3}m$</i>	B2	CsCl	Ref. 8
ε	<i>hP2</i>	<i>P6₃/mmc</i>	A3	Mg	Ref. 9
ε_1	
ε_2	
α'	<i>cP4</i>	<i>Pm$\bar{3}m$</i>	L1 ₂	AuCu ₃	Ref. 8
α'_1	<i>tP2</i>	<i>P4/mmm</i>	L1 ₀	AuCu	Ref. 8
γ	<i>cI52</i>	<i>I$\bar{4}3m$</i>	D8 ₂	γ brass	Ref. 9, 10
γ_1	
δ	
δ_1	...	<i>P6₃/mmc</i>	Ref. 11
ζ	<i>mC28</i>	<i>C2/m</i>	...	CoZn ₁₃	Ref. 12
Zn	<i>hP2</i>	<i>P6₃/mmc</i>	A3	Mg	Ref. 12

Undetermined information is indicated by “... “

α'/α'_1 transition is below 0 °C thus not shown in Fig. 1(a). However, the compositional limit on the Zn-rich side of the α' phase has not been accurately determined.

Schramm et al.^[18] identified the δ phase by conducting thermal analysis and x-ray analyses. Its stable temperature range was between 415 and 462 °C. After that, Wachtel and Tsiuplakis^[13] revised the stable temperature range to 380–462 °C. Currently, Wachtel and Tsiuplakis’ data are adopted. However, the evidence for the existence of the δ phase is considered insufficient because the occurrence of the $\varepsilon_2 + L \rightarrow \delta$ peritectic reaction was assumed based exclusively on a very slight change in the slope of a magnetic susceptibility curve.^[13]

Li et al.^[11] investigated the crystal structure of the δ_1 phase and the phase equilibria in the compositional range above 88Zn at 400 °C via XRD and EPMA/wavelength-dispersive x-ray spectroscopy (WDS), respectively.

The thermodynamic assessment of the Mn-Zn system has been conducted.^[11,27–29] In the calculated phase diagrams, the γ Mn- β Mn two-phase region in the Mn-rich portion is narrower compared to experimental data.^[14] It has also been pointed out the necessity to obtain more information on the boundaries between the δ Mn and β phases and that on the phase separation of the ε phases for an accurate thermodynamic assessment.^[28]

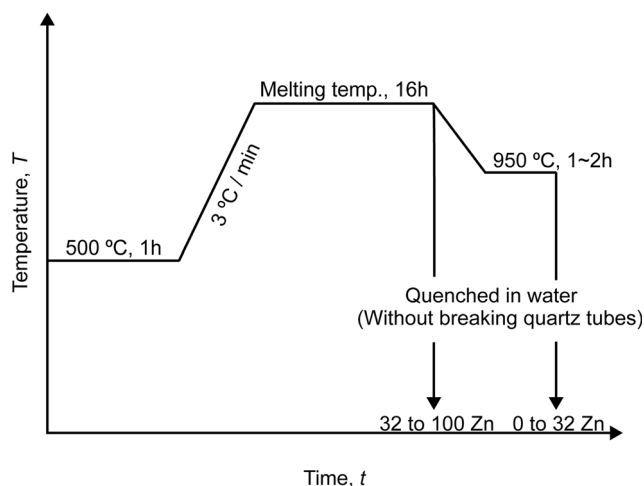


Fig. 2. Heat treatments performed for melting Mn-Zn alloys

3 Experimental Procedure

3.1 Alloy Preparation

Mn-Zn alloys with compositions expressed in at.% were prepared from high-purity Mn flakes (purity 99.9%, produced by South Manganese Group Ltd.), and Zn granules (purity 99.99%, produced by Kojundo Chemical Laboratory Co., Ltd.). The raw materials of Mn and Zn materials

Table 2 Equilibrium compositions in the Mn-rich region determined via FE–EPMA/WDS

Equilibrium phases		Nominal Composition (at.% Zn)	Melting temperature (°C)	Final heat-treatment condition		Equilibrium composition (at.% Zn)	
Phase 1	Phase 2			Temperature (°C)	Time	Phase 1	Phase 2
α Mn	β Mn	10	1230	500	21 d	0.7	12.1
		10	1230	400	61 d	1.2	20.5
β Mn	γ Mn	10	1230	800	8 d	6.4	13.5
		15	1230	700	10 d	9.6	19.3
γ Mn	δ Mn	20	1200	900	3 d	17.3	23.4
		25	1200	800	9 d	23.4	27.3
		32	1150	700	13 d	29.4	33.8
γ Mn	ϵ	38	1150	600	8 d	30.7	40.9
β Mn	ϵ	38	1150	525	10 d	23.9	42.0
		32	1150	500	120 d	25.3	44.5
		44	1100	400	120 d	35.6	51.9
δ Mn	Liq.	46	1100	900	1 d	45.2	59.5
δ Mn	ϵ	47.5	1100	800	7 d	45.4	48.3
		41	1100	700	14 d	39.0	43.2

Table 3 Equilibrium compositions of the alloys containing liquid phases determined via FE–EPMA/WDS

Equilibrium phases		Nominal composition (at.% Zn)	Melting temperature (°C)	Final heat-treatment condition		Equilibrium composition (at.% Zn)	
Phase 1	Phase 2			Temperature (°C)	Time (d)	Phase 1	Phase 2
ϵ	Liq.	58	1050	800	3	55.6	68.9
		70	900	700	5	66.9	78.6
		80	800	600	7	77.4	88.2
		88	800	500	21	85.4	94.9
		92	700	450	42	89.9	97.7

Table 4 Equilibrium compositions in the Zn-rich region determined via FE–EPMA/WDS

Equilibrium phases		Nominal composition (at.% Zn)	Melting temperature (°C)	Final heat-treatment condition		Equilibrium composition (at.% Zn)	
Phase 1	Phase 2			Temperature (°C)	Time (d)	Phase 1	Phase 2
ϵ	α'	66*	900	300	31	64.6	71.1
ϵ	γ	75*	850	380	40	75.0	76.9
		75*	850	360	7	74.5	76.7
α'	γ	76	850	300	21	75.3	79.0
γ	ϵ	83*	800	360	7	82.9	85.3
γ	δ_1	83	800	300	35	82.7	88.3
		ϵ	δ_1	88	800	400	42
δ_1	ζ	86*	800	360	7	85.6	88.8
		91.6	700	400	42	91.4	91.8
		91.6*	700	360	7	91.2	91.9
ζ	Zn	91.6*	700	300	98	90.8	92.1
		94	700	400	42	92.2	99.0
		94*	700	300	98	92.4	99.3

The nominal compositions marked by “*” indicate the use of powdered samples.

were encapsulated in quartz tubes and backfilled with a gas mixture containing 95 vol.% Ar and 5 vol.% H₂. The alloys were melted using a two-step melting method as shown in Fig. 2 and Tables 2, 3, and 4. For compositions with 0 to 32 Zn, the alloys' melting points are high thus we added a third step at 950 °C to minimize the risk of the explosion of quartz tubes during rapid cooling. After melting, each quartz tube was cooled in ice water without breaking. In addition, because the specimens that contained less than 30Zn could react with the quartz tubes at temperatures above 1000 °C, they were placed in Tammann tubes (Al₂O₃, 99.6%) before encapsulation. By conducting the above-mentioned procedure, homogeneous Mn-Zn alloys with different compositions were successfully prepared.

3.2 Preparation of DCs

Two DCs (82Zn/100Zn and 50Zn/75Zn) were prepared from either pure materials or homogeneous alloys. The obtained samples were cut into disks and the surfaces polished. Two disks were mechanically joined with a molybdenum jig. These samples, together with the molybdenum jig, were encapsulated with Ti getters in quartz tubes backfilled with argon gas. Heat treatments to join the diffusion couples were performed at 400 and 500 °C for 2 hours. After that, the joint DCs were encapsulated in quartz tubes backfilled with argon gas and heat-treated at 450 °C for 15 h (82Zn/100Zn) or 28 d (50Zn/75Zn), followed by quenching in ice water. Note the pure Zn in the 82Zn/100Zn DC melts at 450 °C; thus a shorter heat-treatment time was used.

3.3 Heat Treatments for Phase Equilibrium Studies

The prepared Mn-Zn alloys were cut and encapsulated in quartz tubes backfilled with Ar gas. After that, the specimens were heat treated at temperatures between 300 and 800 °C followed by quenching in ice water, as shown in Tables 2, 3, and 4. For improved homogeneity, the samples

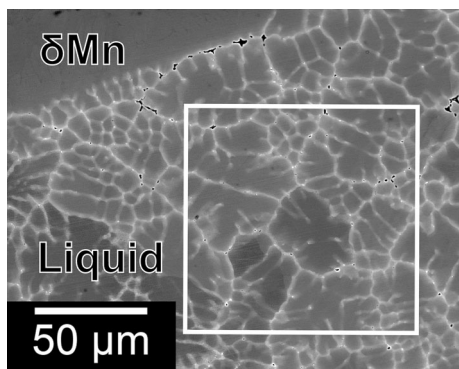


Fig. 3. BSE image of the 46Zn alloy heat-treated at 900 °C for 1 d

with compositions of 50-74Zn were heat-treated at 600 °C for 7 d. Likewise, 80-90Zn were heat-treated at 400 °C or 450 °C for 42 d before the low-temperature heat treatments. At temperatures below 400 °C, since it is more difficult to reach the equilibrium state, when necessary, strain was introduced by mechanically powdering the samples using a stainless steel mortar, so that the dislocation pipe diffusion phenomenon can greatly reduce the time required for equilibration. For the powdered samples, after heat treatments, quenching in ice water was conducted without breaking the quartz tubes.

3.4 Determination of Binary Phase Diagram

3.4.1 Equilibrium Compositions

The equilibrium compositions of the samples and composition profiles of the DCs were determined by field-emission electron probe microanalyzers (FE-EPMA: JEOL JXA-8500F and JEOL JXA-8530F) equipped with WDS at an accelerating voltage of 25 kV and a beam current of 10 nA. During the FE-EPMA measurements, more than seven points per phase were analyzed, and the obtained values were averaged (except for outliers).

3.4.2 Thermal Analysis at High Temperatures

Thermal analyses were conducted via high-temperature differential scanning calorimetry (DSC, Netzsch DSC-404 and DSC-404C). The fabricated samples were cut and encapsulated in quartz tubes backfilled with 95vol%Ar-5vol%H₂ gas before measurements. In the cases involving

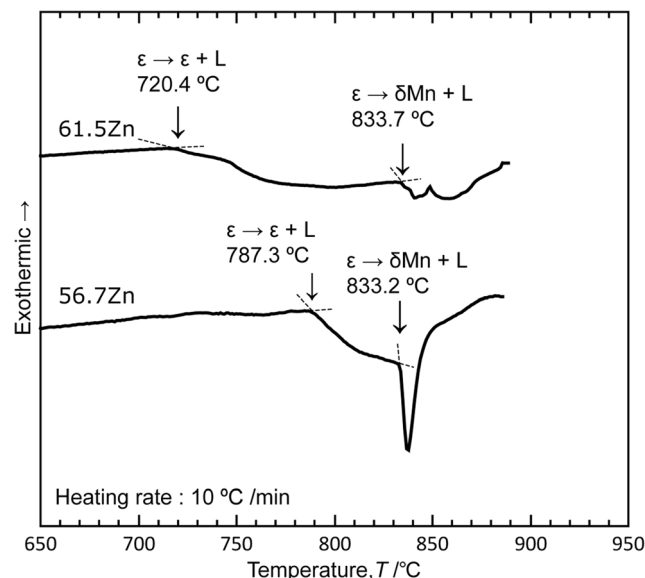
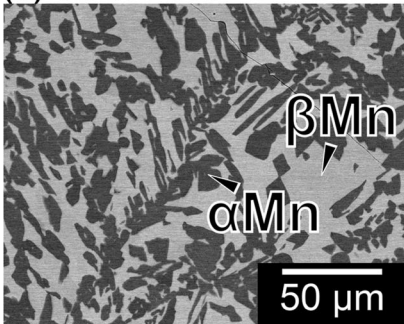


Fig. 4. DSC curves of the 61.5Zn and 56.7Zn alloys recorded at a heating rate of 10 °C/min

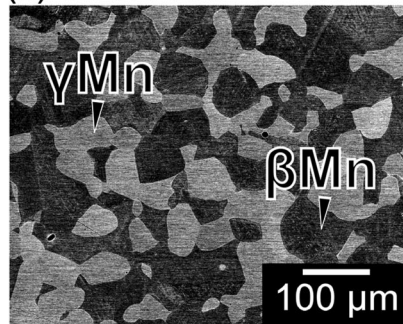
Table 5 Phase transformation temperatures determined via DSC

Nominal composition (at.% Zn)	Temperature (°C)	Transformation during heating
56.7	787.3	$\varepsilon \rightarrow \varepsilon + L$
	833.2	$\varepsilon \rightarrow \delta\text{Mn} + L$
61.5	720.4	$\varepsilon \rightarrow \varepsilon + L$
	833.7	$\varepsilon \rightarrow \delta\text{Mn} + L$
80.3	563.6	$\varepsilon \rightarrow \varepsilon + L$
	680.2	$\varepsilon + L \rightarrow L$
74.7	621.4	$\varepsilon \rightarrow \varepsilon + L$
	737.4	$\varepsilon + L \rightarrow L$
83.2	525.9	$\varepsilon \rightarrow \varepsilon + L$
84.8	497.1	$\varepsilon \rightarrow \varepsilon + L$
86.1	487.1	$\varepsilon \rightarrow \varepsilon + L$
87.8	477.5	$\varepsilon \rightarrow \varepsilon + L$
88.6	465.0	$\varepsilon \rightarrow \varepsilon + L$
90	454.5	$\varepsilon \rightarrow \varepsilon + L$
92.8	414.3	$\zeta + \text{Zn} \rightarrow L$
	427.4	$\zeta \rightarrow \varepsilon + L$
94.6	414.6	$\zeta + \text{Zn} \rightarrow L$
	427.0	$\zeta \rightarrow \varepsilon + L$

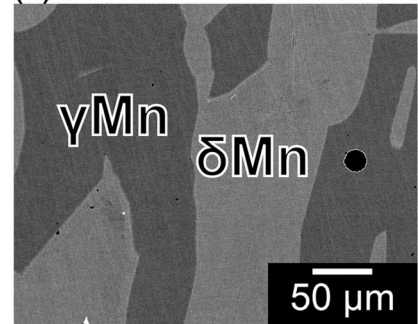
(a) 10Zn : 400 °C × 61d



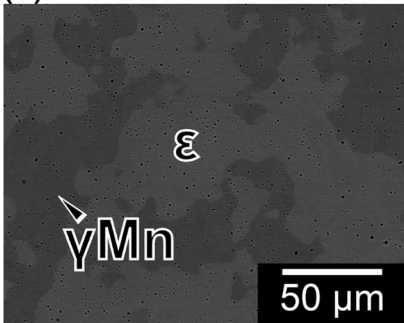
(b) 10Zn : 800 °C × 8d



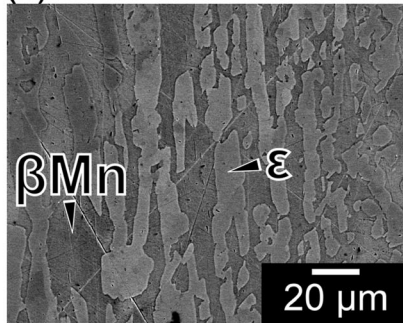
(c) 25Zn : 800 °C × 9d



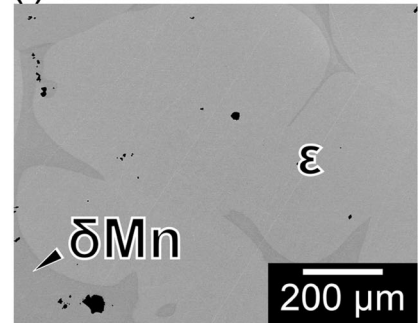
(d) 38Zn : 600 °C × 8d



(e) 44Zn : 400 °C × 120d



(f) 47.5Zn : 800 °C × 7d

**Fig. 5.** BSE images of the (a) 10Zn alloy heat-treated at 400 °C, (b) 10Zn alloy heat-treated at 800 °C, (c) 25Zn alloy heat-treated at 800 °C, (d) 38Zn alloy heat-treated at 600 °C, (e) 44Zn alloy heat-treated at 400 °C, and (f) 47.5Zn alloy heat-treated at 800 °C

liquid phases where a reduced evaporation during measurements is preferred, or in the cases of measurements of second-order transformations where the signals are small, a fast heating rate of 10 °C/min was applied. Otherwise, a slow heating rate of 2 °C/min was used. Before

measurements, a temperature calibration was conducted against the melting points of high purity In (99.999%, $T_m = 156.6$ °C), Sn (99.99%, $T_m = 231.9$ °C), Al (99.999%, $T_m = 660.3$ °C), Ag (99.99%, $T_m = 961.8$ °C), Au (99.999%, $T_m = 1064.2$ °C), and Ni (99.99%,

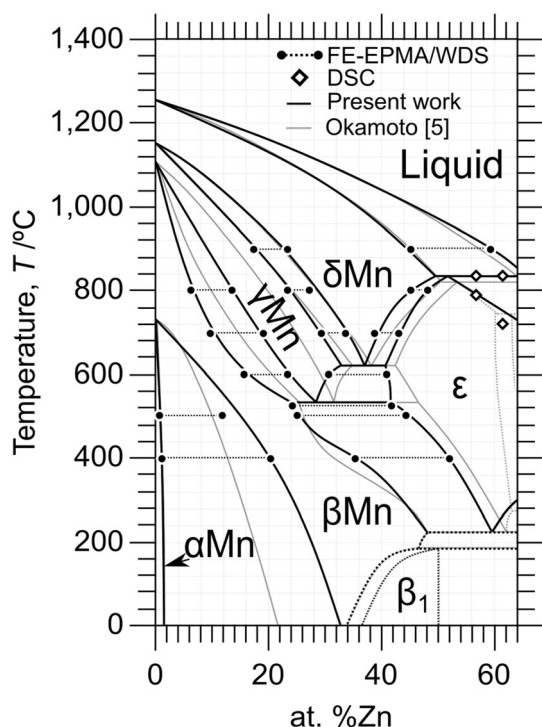


Fig. 6. Mn-rich region of the Mn–Zn binary phase diagram determined experimentally in this study

$T_m = 1455.0$ °C) metals. During the measurements, pure Sn (99.99%, $T_m = 231.9$ °C) was encapsulated in quartz tubes and placed on the reference side of the DSC sample holder. The obtained DSC curves were further calibrated against the melting temperature of Sn to improve the temperature measurement accuracy. All the measurements were conducted under an Ar gas flow using an oxygen trap system (Netzsch OTS®).

3.4.3 Thermal Analysis at Low Temperatures Below 600 °C

Thermal analyses below 600 °C were performed using a low-temperature DSC instrument (Seiko DSC-6200). Samples were placed into aluminum pans (99.9%) and sealed with aluminum lids (99.9%) to suppress vaporization during measurements, which were conducted at a heating condition of 2 °C/min in air. For these measurements no temperature calibration was required because the temperature accuracy, which was verified against the melting points of In and Zn, was sufficiently high.

3.4.4 Crystal Structure Analysis

The crystal structures of the fabricated alloy specimens were investigated via TEM (JEOL ARM-200F) at an accelerating voltage of 200 kV. Samples for analysis were

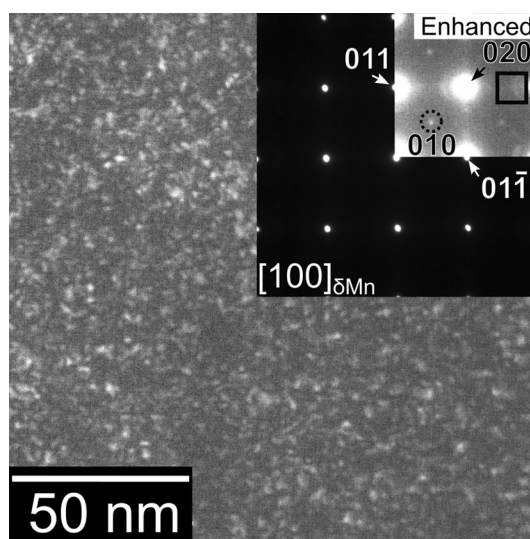


Fig. 7. SADP and dark-field image of the 38Zn alloy heat-treated at 700 °C. The contrast of the upper right quarter of the SADP is enhanced for better visibility of the weak reflection spots

hand polished to a thickness of 100 μm, followed by Ar ion milling processes using an ion slicer (JEOL EM-09100IS). Furthermore, an ion milling system (Fischione M1010) was applied for removing the damaged layer. In addition, to identify the crystal structures, XRD (Rigaku SmartLab) with Cu-K α radiation was performed on the powdered samples.

4 Results and Discussion

4.1 Mn-rich Region

4.1.1 Equilibria Involving the Liquid Phase

The equilibrium compositions of the liquid phase were determined via FE–EPMA/WDS over a wide sample area. Figure 3 shows the backscattered electron (BSE) image of the 46Zn alloy obtained after the heat treatment at 900 °C (The time of heat treatment is noted in Table 2), which consists of the δ Mn and solidified liquid phases. A measurement matrix of 20 \times 20 points on a 100 μm \times 100 μm region was applied, as indicated by the white frame. Since the frozen liquid phase is difficult to obtain because phase separation and segregation occur during solidification, as shown in Fig. 3, the average of the 400 measurement points was treated as the equilibrium composition of the liquidus, which is 59.5Zn; this value is close to that determined by Romer and Wachtel (about 56.2Zn).^[14] Additionally, FE-EPMA/WDS spot analyses were also conducted on the δ Mn phase to obtain the solidus

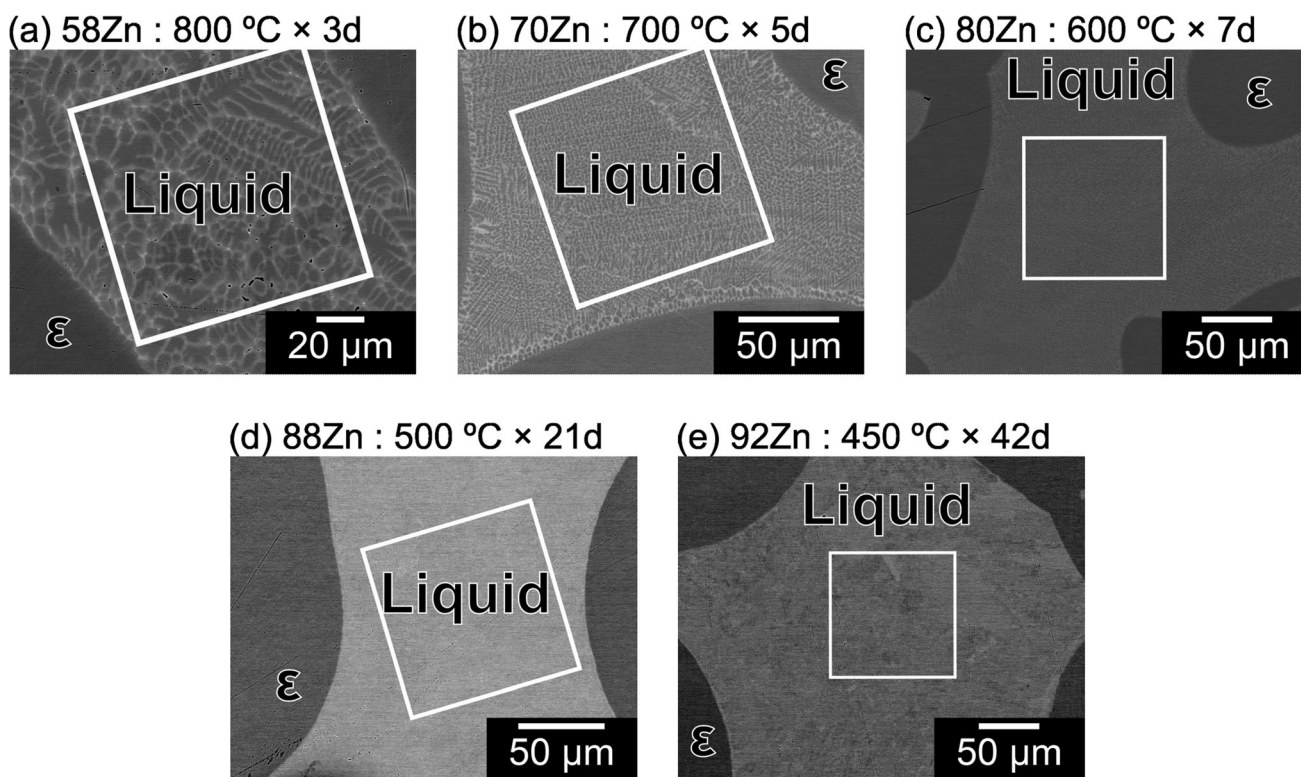


Fig. 8. BSE images of the (a) 58Zn alloy heat-treated at 800 °C, (b) 70Zn alloy heat-treated at 700 °C, (c) 80Zn alloy heat-treated at 600 °C, (d) 88Zn alloy heat-treated at 500 °C, and (e) 92Zn alloy heat-treated at 450 °C

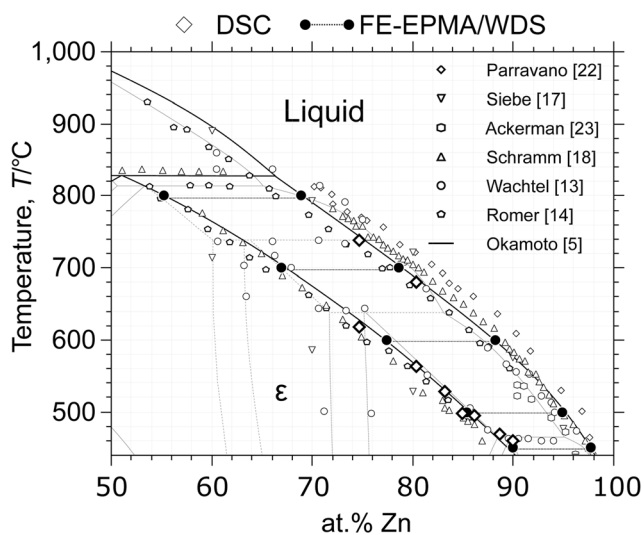


Fig. 9. Partial phase diagram of the Mn–Zn binary system with the liquid phase determined experimentally in this study

composition (45.0Zn), which was similar to the value reported by Romer and Wachtel (about 43.8Zn).^[14]

So far, the reported invariant reaction temperatures of $\delta\text{Mn} + \text{L} \rightarrow \varepsilon$ differ in literature. In the present study, we used thermoanalysis to determine this temperature. The DSC profiles of 61.5Zn and 56.7Zn are shown in Fig. 4, and the measured transformation temperatures are listed in

Table 5. Gradual endothermic signals can be recognized, corresponding to the solidus temperatures of 720.4 °C for 61.5Zn and 787.3 °C for 56.7Zn. The sharp endothermic peaks of both samples are located at 833.7 °C and 833.2 °C; these peaks correspond to the peritectic invariant reaction $\delta\text{Mn} + \text{L} \rightarrow \varepsilon$, and their temperatures are slightly lower than the value reported by Schramm (835 °C).^[18] Thus, the peritectic temperature was determined as 833.5 °C in this study by taking the average.

4.1.2 Phase Equilibria Between Mn-rich Phases

Figure 5(a)–(f) show the BSE images of the Mn-rich alloys. Each microstructure contains two phases coarsened to sizes over 10 μm, which is sufficient for analysis using FE–EPMA/WDS. Note that the different contrast in single phases seen in Fig. 5(b) is caused by difference in crystal orientation. Equilibrium compositions are summarized in Table 2 and plotted as the circles in Fig. 6. The obtained results indicate that the αMn – βMn two-phase region is significantly wider than that reported by Okamoto and Tanner.^[5] However, the results are in good agreement with Romer and Wachtel’s study which reported the phase boundary of the $\alpha\text{Mn} + \beta\text{Mn}/\beta\text{Mn}$ occurs within 18Zn to 20Zn at 400 °C and 12Zn to 14Zn at 500 °C.^[14] Also, Romer and Wachtel employed thermal analysis during the

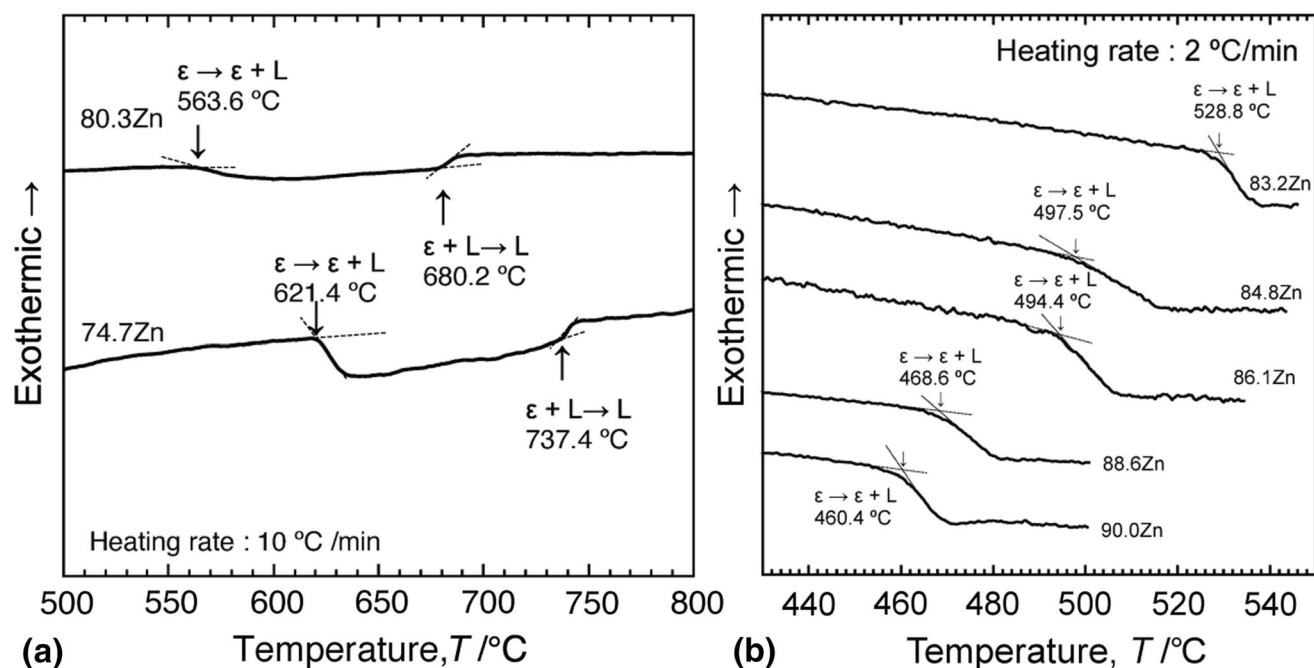


Fig. 10. DSC curves of the (a) 80.3Zn and 74.7Zn alloys obtained at a heating rate of 10 °C/min and (b) 83–90 Zn alloys obtained at a heating rate of 2 °C/min

heating process to determine the two-phase region between β Mn and γ Mn phases. Their determined temperatures for both the β Mn/ β Mn + γ Mn and the β Mn + γ Mn/ γ Mn boundaries are generally higher than those in the present study, which is probably due to slow diffusion in the Mn-rich alloys that have high melting temperature.

4.1.3 Crystal Structure of the β Phase

In this study, the crystal structure of the β phase, which was previously determined as the B2 structure, was investigated for the 38Zn alloy. The alloy was heat-treated at 700 °C for 1 d and then quenched in ice water. The inset of Fig. 7 shows its selected area diffraction pattern (SADP), with the upper right quarter enhanced for a better visibility of weak reflection spots. The fundamental spots in the SADP suggest that the current alloy basically has a bcc structure. In addition to the fundamental reflections (such as 011 and 020), very weak satellite reflections were also confirmed, such as the 010 spot and other even weaker extra spots which are indicated by the square. The dark-field image taken from the 010 spot characterizing B2 structure is shown in Fig. 7, where a domain-like structure is observed. The size of the domains is very small, being about 2 to 5 nm, and the fine microstructure may be anti-phase domains or precipitates related to B2, which were most likely formed during the quenching. Therefore, it is most

probable that the current 38Zn alloy shows a single phase with A2 disordered bcc structure at 700 °C, and thus the B2-ordered β phase does not exist in the equilibrium at this temperature. The determined Mn-rich portion of the Mn-Zn binary phase diagram is shown in Fig. 6.

4.2 Zn-rich Region

4.2.1 Equilibria Involving the Liquid Phase

The liquidus and solidus in the Zn-rich region were determined in the same manner as those in the Mn-rich region. Figure 8(a)–(e) show the BSE images of the L + ϵ microstructures of (a) 58Zn at 800 °C, (b) 70Zn at 700 °C, (c) 80Zn at 600 °C, (d) 88Zn at 500 °C, and (e) 92Zn at 450 °C. The areas used for the WDS analyses are indicated by the white frames. Their average compositions are listed in Table 3 and plotted in Fig. 9.

A thermal analysis was performed to confirm the reliability of the conducted measurements. The solidus and liquidus temperatures determined for the 80.3Zn and 74.7Zn compositions are shown in Fig. 10(a). In addition, the solidus temperatures of the Zn-rich compositions are displayed in Fig. 10(b). The results presented in Fig. 9 and Table 5 are in good agreement with the WDS analysis data described above and are also close to literature values such as those reported by Schramm.^[18]

4.2.2 Phase Separation Within the ε Phase

As shown in Fig. 1(a), it has been controversial whether a phase separation exists within the ε phase, and thus whether

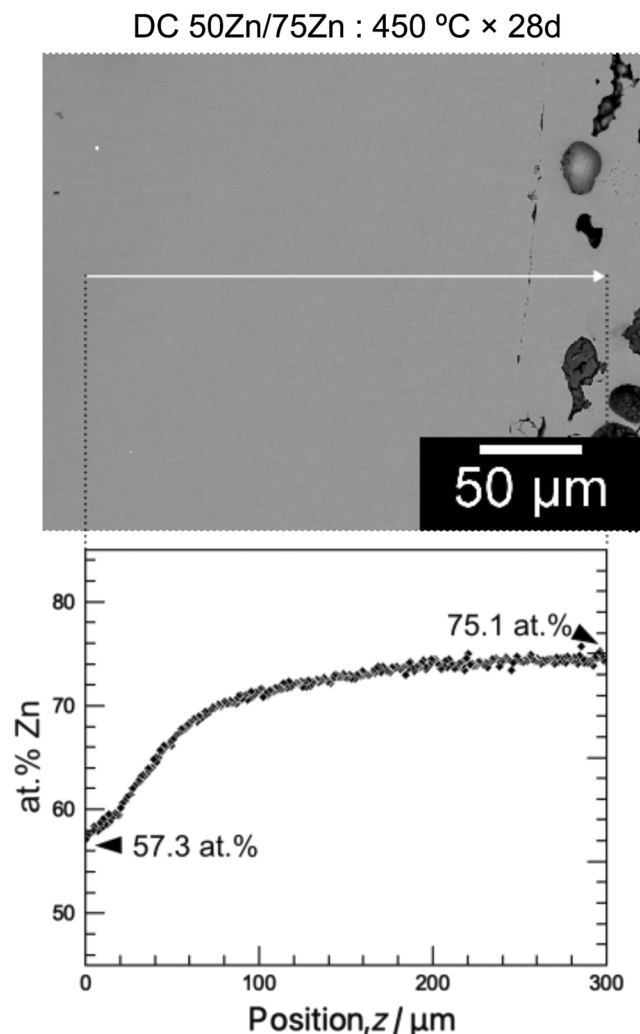
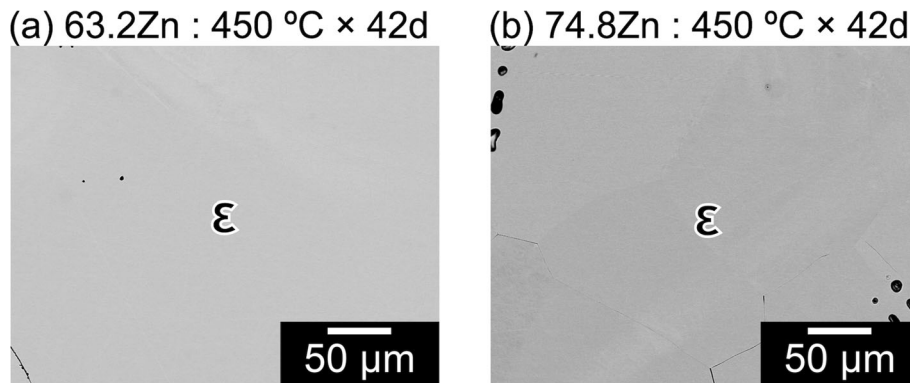


Fig. 11. BSE images and composition profiles of the 50Zn/75Zn DC heat-treated at 450 °C for 28 d

Fig. 12. BSE images of the (a) 63.2Zn and (b) 74.8Zn alloys heat-treated at 450 °C for 42 d



the ε_1 and ε_2 phases exist. In the present study, this was investigated using a DC and several alloys. The DC was prepared by joining the 50Zn and 75Zn alloys at 500 °C for 2 h followed by a heat treatment at 450 °C for 28 d. Fig. 11 shows the microstructure and diffusion profile of the 50Zn / 75Zn DC. The diffusion profile corresponds to the composition range covering the previously reported two-phase regions between the ε , ε_1 , and ε_2 phases. If such regions existed, discontinuous changes in the composition would be observed in the ranges of 62–65Zn and 72–76Zn. However, the composition profile between 57.3Zn and 75.1Zn is smooth indicating the absence of two-phase regions. Furthermore, two alloys with the compositions 63.2Zn and 74.8Zn were prepared and heat treated at 450 °C for 42 d. These compositions are located inside the previously reported two-phase regions between the $\varepsilon + \varepsilon_1$

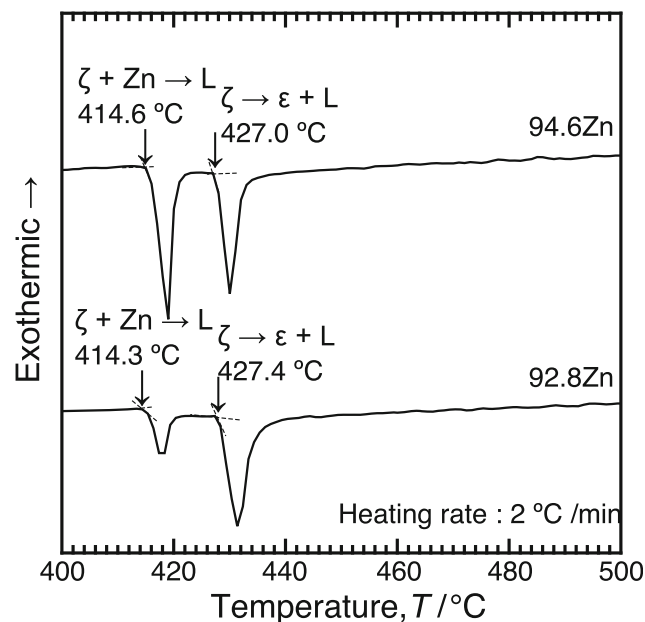
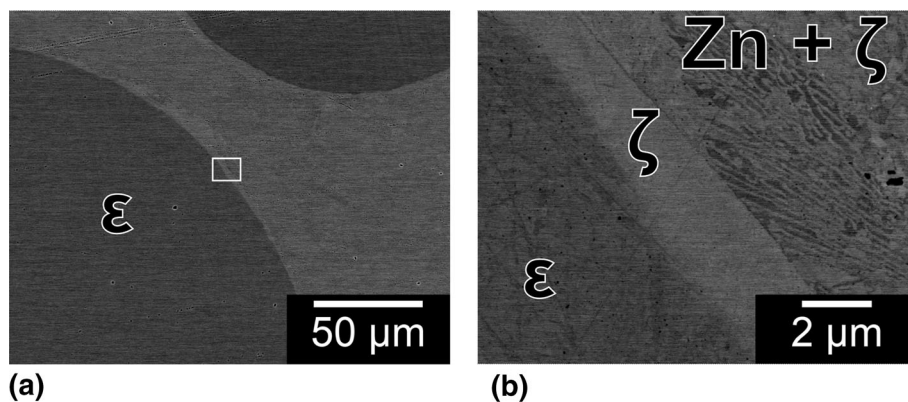


Fig. 13. DSC curves of the 94.6Zn and 92.8Zn alloys recorded at a heating rate of 2 °C/min

Fig. 14. BSE images of the 94.0 Zn alloys heat-treated at 450 °C for 42 d. (a) Low magnification image. (b) High magnification image of the area indicated by the frame in (a)



DC 82Zn/100Zn : 450 °C × 15h

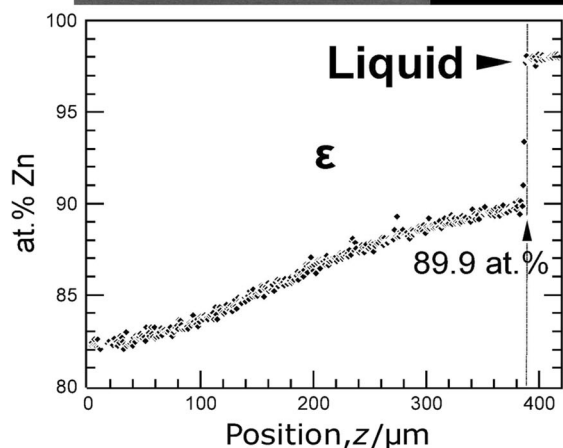
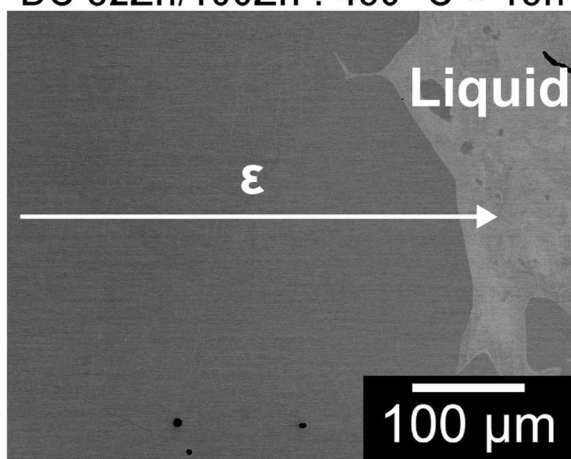


Fig. 15. BSE images and composition profiles of 82Zn/100Zn DC heat-treated at 450 °C for 15 h

and $\varepsilon_1 + \varepsilon_2$ phases. As shown in Fig. 12(a) and (b), both samples contain single phases. From these results, we have concluded that the single-phase region of the ε phase has a wide compositional span, whereas the ε_1 and ε_2 phases do not exist.

4.2.3 Thermal Analysis of the Zn-Rich Region and Absence of the δ Phase

Figure 13 shows the thermal-analysis curves of the 94.6Zn and 92.8Zn alloys. Their eutectic $L \rightarrow \zeta + \text{Zn}$ reaction occurs at 414.6 °C and 414.3 °C, respectively. The eutectic temperature obtained by averaging these two values is equal to 414.5 °C, which is slightly lower than that reported by Li et al. (418 °C).^[11] Similarly, the peritectic temperature of $\varepsilon + L \rightarrow \zeta$ is 427.2 °C. In contrast to the results of previous studies,^[13,18] the peaks related to the $L + \varepsilon \rightarrow \delta$ reaction are not present in the temperature range of 400–500 °C. To confirm the interpretation of the thermal analysis, we examined the microstructure of a 94.0Zn alloy, which was heat-treated at 450 °C for 42 days and then water-quenched (Fig. 14). According to the WDS analysis, the phase identified as ε phase is composed of 90.0Zn, and the ζ phase is composed of 92.7Zn. This indicates that the primary ε phase and peritectic microstructure of ζ phases formed upon the peritectic reaction of $\varepsilon + L \rightarrow \zeta$ (Fig. 14a). Additionally, a eutectic microstructure consisting of $\text{Zn} + \zeta$ is also confirmed, being evidence for the reaction $L \rightarrow \zeta + \text{Zn}$ (Fig. 14b). To verify the existence of a two-phase region between the ε and δ phases, we prepared a DC by joining the 82Zn alloy and pure Zn at 400 °C for 2 h. Heat treatment was conducted at 450 °C for 15 h, and the obtained DC microstructure and diffusion profile are shown in Fig. 15. A continuous change in the DC composition is observed from 82.0Zn to 89.9Zn, suggesting the absence of any two-phase regions. In addition, microstructural observations (Figs. 16a–c) and x-ray analyses (Fig. 17) were conducted to identify the crystal structure for the 86.0Zn, 87.9Zn, and 88.6Zn alloys heat-treated at 450 °C for 42 d without employing Rietveld analysis. Note that the different contrast in single phases seen in Fig. 16(c) is caused by difference in crystal orientation. All these samples contain in single phases with the hcp structures. Thus, it can be concluded that the δ phase does not exist in the Mn–Zn

Fig. 16. BSE images of the (a) 86.0Zn, (b) 87.9Zn, and (c) 88.6Zn alloys heat-treated at 450 °C for 42 d

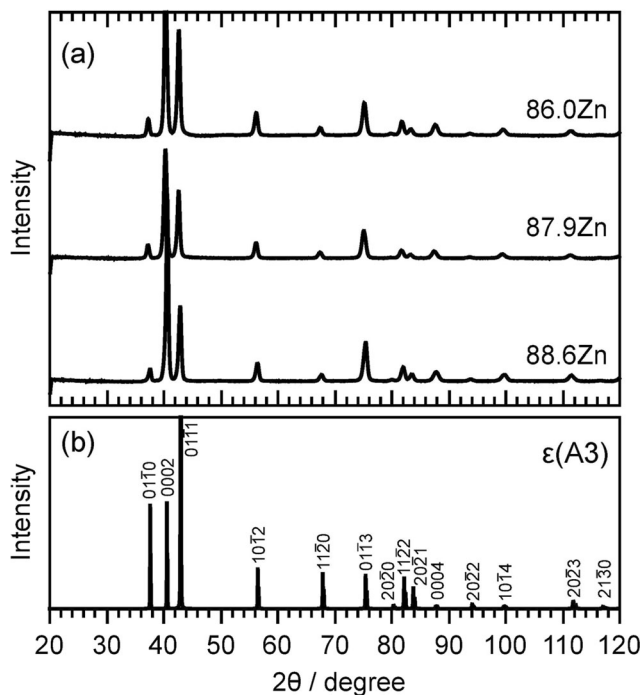
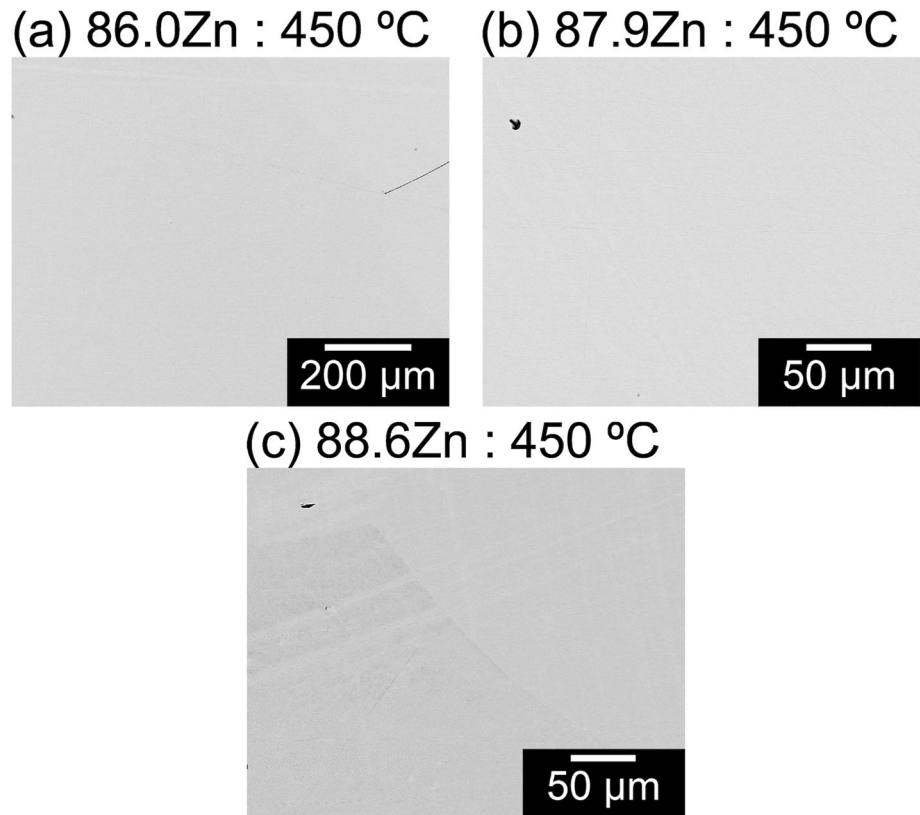


Fig. 17. (a) Powder XRD patterns of the 86.0Zn, 87.9Zn, and 88.6Zn alloys heat-treated at 450 °C for 42 d. (b) Calculated XRD patterns of the ϵ phase

binary system, which is reflected in the updated phase diagram, as shown in Fig. 18(a) and (b).

4.2.4 Equilibrium Thermal Analysis and Chemical Composition Analysis for Other Solid Phases

Figure 19(a)-(h) shows the microstructures of the alloys heat-treated at temperatures between 300 and 800 °C. In these experiments, we used mechanically powdered specimens at temperatures below 400 °C because the diffusion in these specimens was very slow. Their chemical compositions are summarized in Table 4 and plotted in Fig. 18(a) and (b) with the phase diagrams determined previously by Okamoto and Tanner^[5] and Li et al.^[11], respectively. The two-phase region between the α' and ϵ phases is wider than that in Okamoto and Tanner's version^[5] based on Wachtel and Tsiuplakis' experimental data.^[13] Therefore, the γ , δ_1 , and ζ phases exhibit narrower composition ranges at lower temperatures.

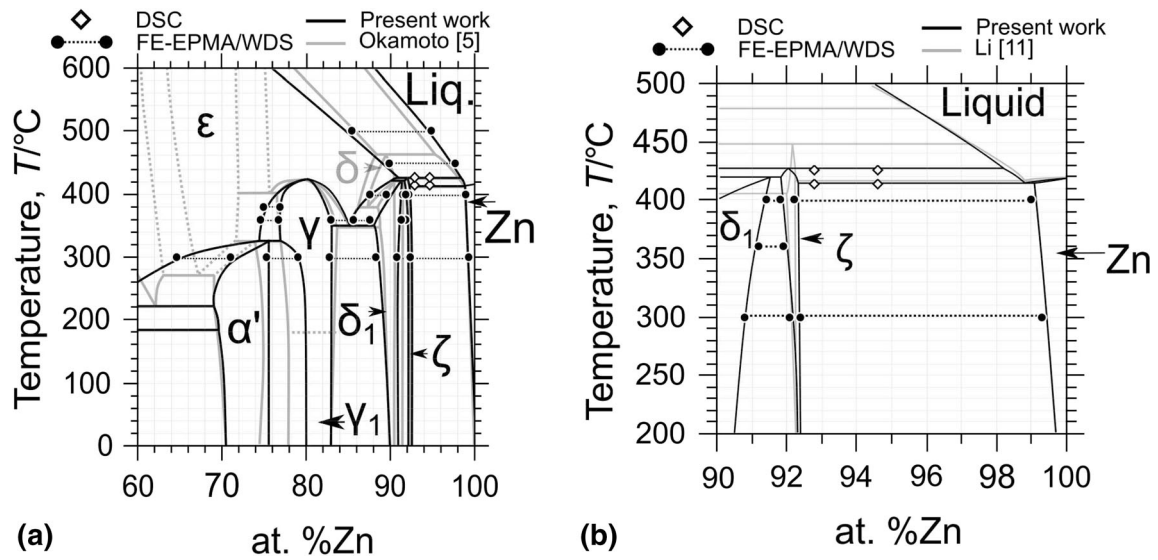


Fig. 18. Partial phase diagram of the (a) 60-100Zn and (b) 90-100Zn portions of the Mn-Zn binary system determined experimentally in this study

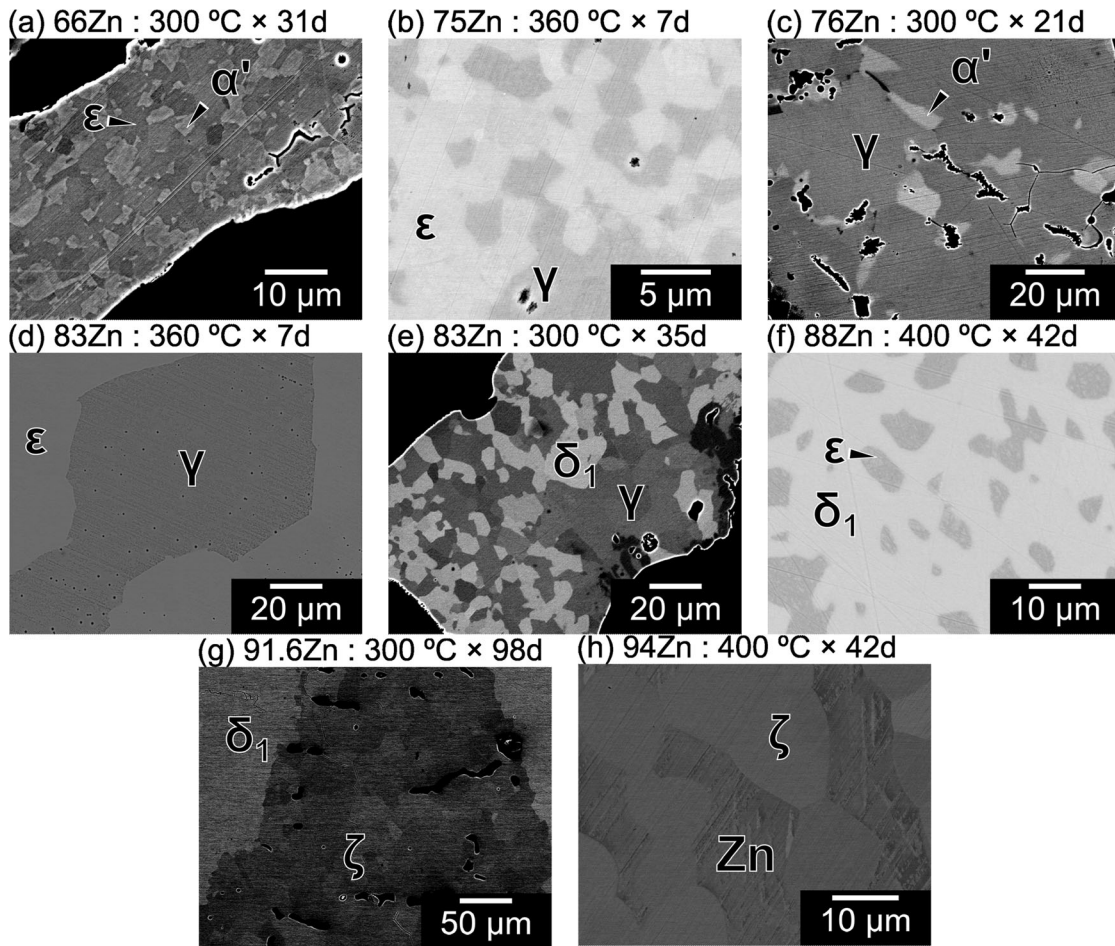


Fig. 19. BSE images of the (a) 66Zn powdered sample heat-treated at 300 °C, (b) 75Zn powdered sample heat-treated at 360 °C, (c) 76Zn powdered sample heat-treated at 300 °C, (d) 83Zn powdered sample heat-treated at 360 °C, (e) 83Zn powdered sample heat-treated at 300

°C, (f) 88Zn alloy heat-treated at 400 °C, (g) 91.6Zn powdered sample heat-treated at 300 °C, and (h) 94Zn alloy heat-treated at 400 °C

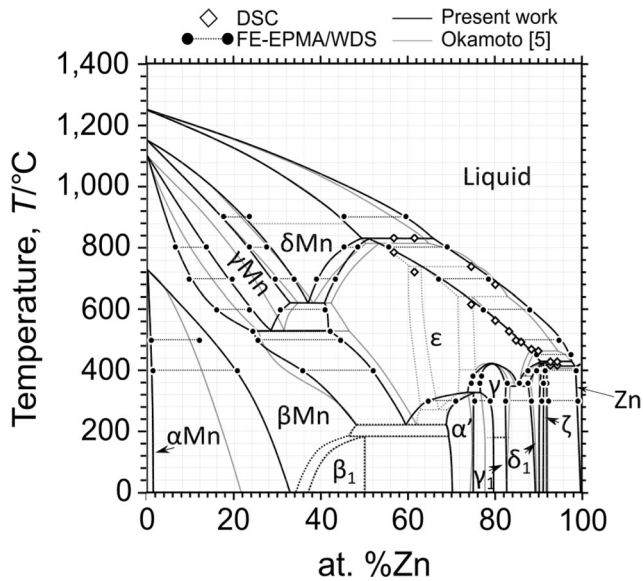


Fig. 20. Final phase diagram of the Mn-Zn binary system was determined experimentally in this study

Table 6 Invariant reaction temperatures determined via DSC

Reaction type	Invariant reaction	Temperature (°C)	References
Peritectic	$\delta\text{Mn} + \text{L} \rightarrow \varepsilon$	833.5	This work
		835	Ref. 18
		815	Ref. 14
Eutectic	$\text{L} \rightarrow \zeta + \text{Zn}$	414.5	This work
		418	Ref. 19
		400	Ref. 20
		416	Ref. 17
		414	Ref. 21
		416	Ref. 18
Peritectic	$\varepsilon + \text{L} \rightarrow \zeta$	417.25	Ref. 30
		416	Ref. 13
		427.2	This work

4.3 Phase Equilibria in the Whole Composition Range

The phase equilibria in the Mn-Zn binary system were experimentally determined via thermal and compositional analyses. The equilibrium compositions and temperatures are plotted in Fig. 20, with the phase boundaries drawn as black lines. For comparison, the phase diagram assessed by Okamoto and Tanner^[5] is shown as gray lines. The invariant temperatures determined by DSC are listed in Table 6. We believe that the redetermined phase diagram can be helpful for a re-assessment of the Mn-Zn binary system, and it can also provide fundamental data for a

thermodynamic assessment of high-order phase diagrams such as Fe-Mn-Zn in the future.

5 Summary

The major findings of this study are summarized as follows:

- In the Mn-rich region, a single γMn phase was determined on the Mn-rich side.
- According to the TEM and thermal analysis data, the $\beta\text{-B2}$ phase was not confirmed in the equilibrium phase diagram.
- Based on the WDS analysis results obtained for the DC and alloy microstructure, a phase separation within the ε phase did not occur.
- According to the results of the thermal and WDS analyses of the DC, microstructural observations, and crystal structures, the δ phase was not detected in the studied alloys.
- The α' and ε phases formed wide two-phase regions. The composition range between the δ_1 and ζ phases was narrower than that reported previously.

Acknowledgment This study was supported by the JST FOREST Program (grant number JPMJFR203B) and a JSPS KAKENHI (grant number JP22K18877). Part of this work was performed at the Research Center for Rare Metal and Green Innovation (RaMGI), Tohoku University, which was established with the support of the Ministry of Economy, Trade, and Industry (METI) and Ministry of Education, Culture, Sports, Science and Technology (MEXT).

Open Access This article is licensed under a Creative Commons Attribution 4.0 International License, which permits use, sharing, adaptation, distribution and reproduction in any medium or format, as long as you give appropriate credit to the original author(s) and the source, provide a link to the Creative Commons licence, and indicate if changes were made. The images or other third party material in this article are included in the article's Creative Commons licence, unless indicated otherwise in a credit line to the material. If material is not included in the article's Creative Commons licence and your intended use is not permitted by statutory regulation or exceeds the permitted use, you will need to obtain permission directly from the copyright holder. To view a copy of this licence, visit <http://creativecommons.org/licenses/by/4.0/>.

References

1. O. Grässel, and G. Frommeyer, Effect of Martensitic Phase Transformation and Deformation Twinning on Mechanical Properties of Fe-Mn-Si-Al Steels, *Mater. Sci. Technol.*, 1998, **14**(12), p 1213–1217.
2. O. Grässel, L. Krüger, G. Frommeyer, and L.W. Meyer, High Strength Fe-Mn-(Al, Si) TRIP/TWIP Steels Development-Properties-Application, *Int. J. Plast.*, 2000, **16**, p 1391–1409.

3. S. Vercaemmen, B. Blanpain, B.C. de Cooman, and P. Wollants, Cold Rolling Behaviour of an Austenitic Fe-30Mn-3Al-3Si TWIP-Steel: The Importance of Deformation Twinning, *Acta Mater.*, 2004, **52**(7), p 2005–2012.
4. G. Reumont, G. Dupont, and P. Perrot, The Fe-Zn-Mn System at 450 °C, *Z. Metallkd.*, 1995, **86**(9), p 608–613.
5. H. Okamoto, and L.E. Tanner, The Mn-Zn (Manganese-Zinc) System, *Bull. Alloy Phase Diagrams*, 1990, **11**(4), p 377–383.
6. P. Villars, and L.D. Calvert, *Pearson's Handbook of Crystallographic Data for Intermetallic Phases*, Vol. 3. ASM International, Materials Park, 1985, p2710
7. Y. Nakagawa, S. Sakai, and T. Hori, Magnetic Properties of Mn-Zn Alloys, *J. Phys. Soc. Jpn.*, 1962, **17**, p 168–171.
8. Y. Nakagawa, and T. Hori, Neutron Diffraction Studies of Mn-Zn Alloys, *J. Phys. Soc. Jpn.*, 1964, **19**(11), p 2082–2087.
9. N. Parravano, and V. Caglioti, Stuttura e Composizione Chimica di Alcune Leghe Metallliche, *Mem. R. Accad. Ital. Cl. Sci. Fis. Mat. Nat. Chim.*, 1932, **3**(3), p 5–21. (in Italian)
10. S. Eveland, S. Thiminaiah, M.G. Marshall, and G. Miller, Γ -Brasses in the Mn-Zn System: An Experimental and Computational Study, *J. Solid State Chem.*, 2019, **269**, p 297–304.
11. X. Li, S. Liu, J. Huang, D. Huang, and Y. Du, Phase Equilibria, Crystal Structure of δ_1 -MnZn₉ and Thermodynamic Re-assessment of the Zn-Mn System, *J. Alloys Compd.*, 2021, **863**, p 158484.
12. P. Villars, *Crystallographic Data for Intermetallic Phases Pearson's Handbook Desk Edition*, Vol. 2. ASM International, Materials Park, 1997, p2396–2886
13. E. Wachtel, and K. Tsiuplakis, Magnetische Eigenschaften Zinkreicher Zink-Mangan-Legierungen im Festen und Geschmolzenen Zustand, *Z. Metallkd.*, 1967, **58**(1), p 41–45. (in German)
14. O. Romer, and E. Wachtel, Zum Aufbau der Systeme Zink-Mangan und Zink-Mangan-Aluminium, *Z. Metallkd.*, 1971, **62**(11), p 820–825. (in German)
15. Y. Nakagawa, and T. Hori, Phase Diagram of Manganese-Zinc System, *Trans. Jpn. Inst. Met.*, 1972, **13**(3), p 167–170.
16. E.V. Potter, and R.W. Huber, Manganese-Zinc Phase Diagram from 0 to 50% Zinc, *Trans. Am. Soc. Met.*, 1949, **41**, p 1001–1023.
17. P. Siebe, Die Legierungen: Mangan-Wismut, Mangan-Zink und Mangan Silber, *Z. Anorg. Allg. Chem.*, 1919, **108**, p 161–183. (in German)
18. J. Schramm, Das System Mangan-Zink von 0 Bis 50% Mn, *Z. Metallkd.*, 1940, **32**(12), p 399–407. (in German)
19. H. Xu, X. Xiong, L. Zhang, Y. Du, and P. Wang, Phase Equilibria of the Mn-Si-Zn System at 600 °C, *Metall. Mater. Trans. A*, 2009, **40**, p 2042–2047.
20. B. Henderson, and R.J.M. Wilcox, Lattice Spacing Relationships in Hexagonal Close-Packed Silver-Zinc-Manganese Alloys, *Philos. Mag.*, 1964, **9**(101), p 829–846.
21. R.A. Farrar, and H.W. King, Axial Ratios and Solubility Limits of H.C.P. η and ϵ Phases in the Systems Cd-Mn and Zn-Mn, *Metallography*, 1970, **3**(1), p 61–70.
22. N. Parravano, and U. Perret, Sulle Leghe di Zinco e Manganese, *Gazz. Chim. Ital.*, 1915, **45**(1), p 1–6. (in Italian)
23. C. Ackermann, Über das Zweistoff-System Mangan-Zink, *Z. Metallkd.*, 1927, **19**(5), p 200–204.
24. G. Edmunds, Liquidus Determinations in Zinc-rich Alloys (Zn-Fe; Zn-Cu; Zn-Mn), *Trans. Metall. Soc. AIME*, 1944, **156**, p 263–276.
25. P. Gieren, Beiträge zur Kenntnis der gegossenen Zink-Legierungen unter Besonderer Berücksichtigung ihrer Verwertung als Lagermetall, *Z. Metallkd.*, 1919, **11**, p 14–22. (in German)
26. H. Uchishiba, T. Hori, and Y. Nakagawa, Cubic-Tetragonal Transition and Antiferromagnetism of α' -MnZn₃, *J. Phys. Soc. Jpn.*, 1969, **27**(3), p 600–604.
27. J. Miettinen, Thermodynamic Description of the Cu-Mn-Zn System in the Copper-rich Corner, CALPHAD: Comput, *Coupling Phase Diagrams Thermochem.*, 2004, **28**(3), p 313–320.
28. X. Li, S. Liu, K. Xu, Y. Zhang, and Y. Du, Thermodynamic Re-assessment and Experimental Confirmation for the Zn-Mn System, CALPHAD: Comput, *Coupling Phase Diagrams Thermochem.*, 2020, **69**, p 101770.
29. X. Li, S. Liu, D. Huang, and Y. Du, Thermodynamic Modeling of the Mg-Mn-Zn System Based on the Refinement of the Mg-Zn and Mn-Zn Systems, CALPHAD: Comput, *Coupling Phase Diagrams Thermochem.*, 2022, **79**, p 102479.
30. E. Weisse, A. Blumenthal, and H. Hanemann, Ergebnisse der Untersuchung Eutektischer Zinklegierungen, *Z. Metallkd.*, 1942, **34**, p 221. (in German)

Publisher's Note Springer Nature remains neutral with regard to jurisdictional claims in published maps and institutional affiliations.